

Final results for mapping the Milky Way’s stellar halo with blue horizontal-branch stars selected from the Subaru Hyper Supreme-Cam Survey

Tetsuya Fukushima^{1,2}, Masashi Chiba², Mikito Tanaka³,
Kohei Hayashi^{4,2,5}, Daisuke Homma^{1,2}, Sakurako Okamoto^{1,6,7},
Yutaka Komiyama³, Masayuki Tanaka^{1,6}, Nobuo Arimoto⁷, and
Tadafumi Matsuno⁸

¹National Astronomical Observatory of Japan, 2-21-1 Osawa, Mitaka, Tokyo 181-8588, Japan
E-mail: t.fukushima@astr.tohoku.ac.jp

²Astronomical Institute, Tohoku University, Aoba-ku, Sendai 980-8578, Japan

³Department of Advanced Sciences, Faculty of Science and Engineering, Hosei University,
184-8584 Tokyo, Japan

⁴National Institute of Technology, Sendai College, Natori, Miyagi 981-1239, Japan

⁵ICRR, The University of Tokyo, 5-1-5 Kashiwanoha, Kashiwa, Japan

⁶The Graduate University for Advanced Studies, Osawa 2-21-1, Mitaka, Tokyo 181-8588,
Japan

⁷Subaru Telescope, National Astronomical Observatory of Japan, 650 North A’ohoku Place,
Hilo, HI 96720, USA

⁸Astronomisches Rechen-Institut, Zentrum für Astronomie der Universität Heidelberg,
Mönchhofstr. 12-14, 69120 Heidelberg, Germany

Received (reception date); Accepted (acceptation date)

Abstract

We select blue-horizontal branch stars (BHBs) from the internal data release of the Hyper Supreme-Cam Subaru Strategic Program to reveal the global structure of the Milky Way (MW) stellar halo. The data are distributed over $\sim 1,100$ deg² area in the range of $18.5 < g < 24.5$ mag, so that candidate BHBs are detectable over a Galactocentric radius of $r \simeq 36 - 575$ kpc. In order to select most likely BHBs by removing blue straggler stars and other contaminants in a statistically significant manner, we develop and apply an extensive Bayesian method, as described in Fukushima et al. (2019). Our sample can be fitted to either a single power-law profile with an index of $\alpha = 4.11^{+0.18}_{-0.18}$ or a broken power-law profile with an index of $\alpha_{\text{in}} = 3.90^{+0.24}_{-0.30}$ at r below a broken radius of $r_{\text{b}} = 184^{+118}_{-66}$ kpc and a very steep slope of $\alpha_{\text{out}} = 9.1^{+6.8}_{-3.6}$ at $r > r_{\text{b}}$; the statistical difference between these fitting profiles is small. Both profiles are found to show prolate shapes having axial ratios of $q = 1.47^{+0.30}_{-0.33}$ and $1.56^{+0.34}_{-0.23}$, respectively. We also find a signature of the so-called “splashback radius” for the candidate BHBs, which can reach as large as $r \sim 575$ kpc, although it is still inconclusive owing to rather large distance errors in this faintest end of the sample. Our results suggest that the MW stellar halo consists of the two overlapping components: the *in situ* inner halo showing a relatively steep radial density profile and the *ex situ* outer halo with a shallower profile, being characteristic of a component formed from accretion of small stellar systems.

Key words: galaxies: Galaxy: halo — Galaxy: structure — stars: horizontal-branch

1 Introduction

The current standard theory of structure formation based on Λ CDM models suggests that galaxies like the Milky Way (MW) have been formed through hierarchical merging/accretion process from small to large scales (White & Rees 1978). While the memory of this past assembly history is weak or disappears in a bulge and disk, it is imprinted in a faint, spatially extended stellar halo surrounding these brightest stellar components (e.g., see reviews, Helmi 2008; Ivezić, Beers & Juric 2012; Feltzing & Chiba 2013; Bland-Hawthorn & Freeman 2014). Individual merging debris of small stellar systems like globular clusters and dwarf galaxies are present in the form of substructures in a stellar halo, including stellar streams in the spatial distribution of stars and separate subcomponents in their velocity and/or phase-space distribution (e.g., Helmi & White 1999; Bullock & Johnston 2005; Cooper et al. 2010; Malhan et al. 2021; Suzuki et al. 2024). The most dominant substructure in the MW stellar halo is made up from the so-called Gaia-Sausage-Enceladus (GSE), which may have been originated from the merging event some 10 Gyr ago (Helmi et al. 2018; Belokurov et al. 2018). Several other substructures have been discovered thanks to precise astrometric data by *Gaia* satellite, and the cross-matching with photometry, spectroscopy and seismology data allows us to identify the stellar population properties of these ancient progenitors (e.g., Helmi 2020; Das et al. 2020; Horta et al. 2021; Matsuno et al. 2022; Horta et al. 2023).

The smooth, global structure of a stellar halo also reflects how a galaxy formed. Indeed, the results of numerical simulation for galaxy formation suggest a relationship of the smooth component of a stellar halo and the past merging history (Bekki & Chiba 2001; Bullock & Johnston 2005; Deason et al. 2014; Pillepich et al. 2014; Grand et al. 2017; Monachesi et al. 2018). For instance, Deason et al. (2014) showed from the simulation results of Bullock & Johnston (2005) that the slope of the density profile for the outer part of a stellar halo depends on the average time of merging: a more recent merging time reveals a shallower radial density profile at the Galactocentric distance, r , beyond 50 kpc. Also, the slope of a stellar halo profile may show a break, and it can be a signature of the past merging event, where a merging progenitor stellar system leaves its debris at its apocenter position (Deason et al. 2018b).

More recent suite of hydrodynamical simulations for galaxy formation by Rodriguez-Gomez et al. (2016) using the Illustris Project shows that the so-called *in situ* halo, i.e., main progenitor halo, shows a steep density profile below a transition radius (roughly $r \sim 50$ kpc for the MW-sized halo), whereas the *ex situ* halo beyond this radius mainly originating from the accretion of small stellar systems exhibits a shallow slope having an outer boundary (see also Rey & Starkenburg 2022 for more details on the dependence on merging histories). Also, based on the magneto-hydrodynamical numerical simulation for galaxy formation named Auriga, Grand et al. (2017) and Monachesi et al. (2018) showed that both the slope in a density profile of a simulated stellar halo and its metallicity gradient are intimately related to the number of main progenitor satellites, which contribute to the total mass of a final halo.

In addition, a sharp jump in the density profile named splashback radius, which is related to the edge of the halo, also plays an important role in elucidating the formation history and mass of galaxies, where stars and/or dark-matter particles reach the apocenter of their first orbit: this physical boundary separates the infalling/accreting material from the halo. For dark matter, Adhikari et al. (2014), Diemer & Kravtsov (2014) and More et al. (2015) explored the density profile and found that the splashback radius falls in the range $0.8 - 1.0 r_{200}$ for rapidly accreting halos, and is $\sim 1.5 r_{200}$ for slowly accreting halos, where r_{200} denotes the virial radius inside which the mean density is 200 times that of the Universe. Deason et al. (2020) mentioned that in the case of an environment like the Local Group, the second jump in the density profile of the star is shown to be more observable. It is thus of great importance to derive the global smooth structure of a stellar halo to infer its merging history.

For this purpose, the stellar halo in the MW is an ideal target, because its three-dimensional distribution is available from several halo tracers, such as red giant-branch stars (RGBs), RR Lyrae (RRLs), blue horizontal-branch stars (BHBs) and blue straggler stars (BSs). These stars are bright enough to map out the stellar halo in the MW up to its outermost edge (e.g., Sluis & Arnold 1998; Yanny et al. 2000; Chen et al. 2001; Sirko et al. 2004; Newberg & Yanny 2005; Jurić et al. 2008; Keller et al. 2008; Sesar et al. 2011; Deason et al. 2011; Xue et al. 2011; Deason et al. 2014; Cohen et al. 2015; Cohen et al. 2017; Vivas et al.

2016; Slater et al. 2016; Xu et al. 2018; Hernitschek et al. 2018; Iorio et al. 2018; Fukushima et al. 2018; Fukushima et al. 2019; Stringer et al. 2021; Yu et al. 2024; Medina et al. 2024; Feng et al. 2024; Amarante et al. 2024). From these studies, the smooth component of the stellar halo can be fitted to a power-law density profile with $r^{-\alpha}$, where α is a power-law index, after the removal of several halo substructures including the Sagittarius stream and the Virgo overdensity (Ibata et al. 1995; Belokurov et al. 2006; Jurić et al. 2008).

Recent large grand-based surveys for BHBs such as Canada-France Imaging Survey (CFIS), Dark Energy Survey (DES), and Subaru/Hyper Suprime-Cam Strategic Program (HSC-SSP) have succeeded to map out the outer regions of the stellar halo beyond $r \sim 40$ kpc (Hernitschek et al. 2018; Deason et al. 2018a; Fukushima et al. 2018; Thomas et al. 2018; Fukushima et al. 2019; Yu et al. 2024). For instance, Thomas et al. (2018) selected BHBs from the CFIS *u*-band imaging data combined with *griz*-band data from Pan-STARRS 1 and showed that the stellar halo represented by a broken power-law profile with an inner/outer slope of 4.24/3.21 at a break radius of 41.4 kpc is the best fitting case out to $r \sim 220$ kpc. More recently, Yu et al. (2024) using DES DR2 *griz* data selected $\sim 2,100$ BHBs and derived α of ~ 4.28 over $20 \lesssim r \lesssim 70$ kpc. The HSC-SSP data were also used for the selection and analysis of BHBs from the *griz* imaging data (Deason et al. 2018a; Fukushima et al. 2018; Fukushima et al. 2019) to derive the stellar halo up to $r \sim 300$ kpc. Fukushima et al. (2019) reported that the smooth stellar halo beyond $r \sim 50$ kpc can be represented as a single power-law model with $\alpha \simeq 3.7$ and an axial ratio of $q \simeq 1.7$ or alternatively a broken power-law model with an inner/outer slope of 2.9/15.0 at a break radius of 160kpc, based on the internal data release of HSC-SSP obtained before 2018 April, which covered over the sky coverage of ~ 550 deg². This work reported here is an extension of our previous work in Fukushima et al. (2019) using the latest (being almost the final) internal release of the HSC-SSP data over the sky area of $\sim 1,100$ deg², i.e., twice as large as the area used in Fukushima et al. (2019), to arrive at the most likely density profile of BHBs in the outermost parts of the halo.

This paper is organized as follows. Section 2 explains the HSC photometry data that we adopt here and the method for the selection of candidate BHBs based on the *griz*-band photometric data from the HSC-SSP survey. In this section, we also describe our Bayesian method for the selection of BHB stars and the derivation of their spatial distribution. In Section 3, we show the results of our Bayesian analysis for the best set of parameters of the spatial distribution of BHB stars. In Section 4, the discussion

of the current results is presented, and our conclusions are drawn in Section 5.

2 Data and Method

2.1 Data

We adopt the imaging data obtained from the HSC-SSP Wide layer covering $\sim 1,100$ deg² in five photometric bands (*g*, *r*, *i*, *z*, and *y*) (Aihara et al. 2018a; Aihara et al. 2018b; Furusawa et al. 2018; Kawanomoto et al. 2018; Komiyama et al. 2018; Miyazaki et al. 2018), where the target 5 σ point-source limiting magnitudes are (*g*, *r*, *i*, *z*, *y*) = (26.5, 26.1, 25.9, 25.1, 24.4) mag. In this work, we utilize the *g*, *r*, *i* and *z*-band data released in 2021 January (internal data release S21A), for the selection of most likely BHBs and the removal of other contaminants as explained below.

In S21A, the data set covers mainly two separate wide fields (Figure 1), i.e., the north and south sides of the Galaxy. The former and latter are named Spring field at $(\alpha_{2000}, \delta_{2000}) = (130^\circ - 230^\circ, (-2^\circ) - 5^\circ)$, and Autumn field at $(\alpha_{2000}, \delta_{2000}) = (330^\circ - 40^\circ, (-7.5^\circ) - 6^\circ)$, respectively (see Table 1). The HSC data are processed with hscPipe 8.5.3 (Bosch et al. 2018), a branch of the Large Synoptic Survey Telescope pipeline (Ivezić et al. 2008; Axelrod et al. 2010; Jurić et al. 2017; Ivezić et al. 2019) calibrated against PS1 DR1 photometry and astrometry (Schlafly et al. 2012; Tonry et al. 2012; Magnier et al. 2013). All the photometry data are corrected for the mean Galactic foreground extinction (Schlafly & Finkbeiner 2011).

In both Spring and Autumn fields, there exist several spatial substructures associated with the Sagittarius (Sgr) stream (Belokurov et al. 2014), which is formed from a tidally disrupting, polar-orbit satellite, Sgr dwarf. Since our aim in this paper is to deduce the structure of the smooth halo component, we exclude the areas including these substructures in the following analysis in a similar way to Fukushima et al. (2018) and Fukushima et al. (2019).

As shown in Figure 1, the areas, where globular clusters (Harris 1996), dwarf galaxies (McConnachie 2012), and stellar streams have been identified, are excluded from the data to be analyzed.

2.2 Selection of targets

As shown in Fukushima et al. (2019), we select point sources using the *extendedness* parameter from the pipeline, namely *extendedness*= 0 for point sources and *extendedness*= 1 for extended images like galaxies. This parameter is computed based on the ratio between PSF and cmodel fluxes (Abazajian et al. 2004), where a

Table 1. Observed Regions with HSC-SSP

Region	RA (deg)	DEC (deg)	Adopted area (deg ²)
Spring field	130 – 230	(–2) – 5	~ 699
Autumn field	330 – 40	(–7.5) – 6	~ 559
HECTOMAP	200 – 250	42 – 45	~ 109
AEGIS	213 – 216	51.7 – 53.3	2.5

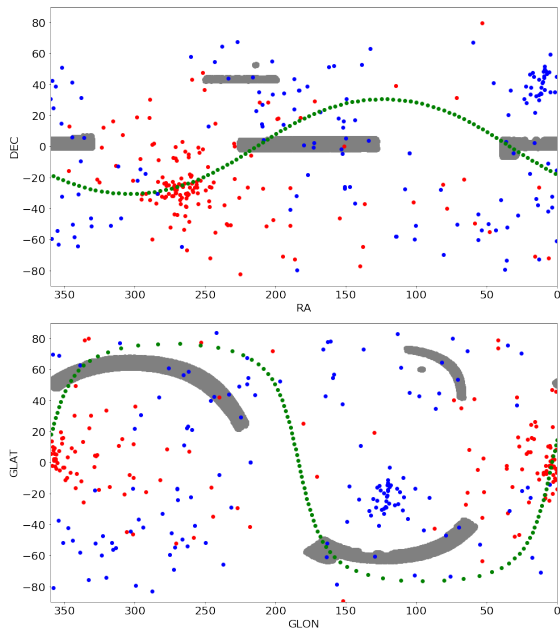


Fig. 1. Upper and middle panels show observed areas of HSC-SSP S21A Wide layer (black shaded regions), compared with the distributions of globular clusters (red dots: Harris (1996)) and dwarf galaxies (blue dots: McConnachie (2012)). The green dots trace the Sagittarius stream (Belokurov et al. (2014)).

point source is defined to be an object having this ratio larger than 0.985. As shown in Aihara et al. (2018b), this star/galaxy classification becomes uncertain for faint sources. Therefore, we probabilistically handled the influence of galactic contamination using the function shown in Fig.1 of Fukushima et al. (2019).

We then select point sources in the following magnitude and color ranges:

$$\begin{aligned}
 &18.5 < g < 24.5 \\
 &-0.3 < g - r < 0 \\
 &-0.4 < r - i < 0.4 \\
 &-0.25 < i - z < 0.1,
 \end{aligned} \tag{1}$$

where the faint limit for the g -band magnitude range is taken based on its photometric error of typically $\simeq 0.05$ mag with maximum of $\simeq 0.1$ mag.

These point sources include not only BHBs but also other point sources including BSs, WDs and QSOs, with

some amount of faint galaxies which are misclassified as stars. As demonstrated in Fukushima et al. (2018), BHBs are distributed in the distinct region in the $i - z$ vs. $g - r$ diagram, because the $i - z$ color is affected by the Paschen features of stellar spectra and is sensitive to surface gravity (Lenz et al. 1998; Vickers et al. 2012). Thus, other A-type stars having higher surface gravity, i.e. BSs, as well as white dwarfs (WDs) can be excluded based on their distributions in the $i - z$ vs. $g - r$ diagram. Since quasars (QSOs) are largely overlapping with BHBs in this diagram, the removal of these point sources also requires the use of the $r - i$ vs. $i - z$ diagram.

2.3 Probability distributions of BHBs, BSs, WDs, QSOs and galaxies in the color-color diagrams

This paper adopts a Bayesian method for the selection of BHB stars as shown in Fukushima et al. (2019). In this method, the likely distributions for each of BHBs, BSs, WDs, QSOs and faint galaxies in the color-color diagrams defined by g , r , i and z -band are assembled and analyzed.

For this purpose, we perform a crossmatching between the HSC-SSP data and the corresponding datasets for these objects taken from several other works, i.e., WDs taken from Kleinman et al. (2013); Kepler et al. (2015); Kepler et al. (2016), QSOs obtained in Pâris et al. (2018)¹. After this crossmatching with HSC-SSP, we obtain 401 WDs and 3705 QSOs.

To get probability distributions of BHBs and BSs, we use the same samples as in Fukushima et al. (2019), which utilized the data provided from SEGUE (Sloan Extension for Galactic Understanding and Exploration) Stellar Parameter Pipeline (SSPP: Lee et al. 2008).

We then set the constraints of $3.0 < \log(g) < 3.75$ for BHBs and $3.75 < \log(g) < 4.5$ for BSs, which well separate the both stellar populations. The constraints for this selection are similar to those in Vickers et al. (2012), which set $3.0 < \log(g) < 3.75$ for BHBs and $3.75 < \log(g) < 5.0$ for BSs.

For galaxies as remaining contaminants, we use the HSC-SSP data with *extendedness*=1, corresponding to extended images.

¹ http://www.sdss.org/dr14/algorithms/qso_catalog

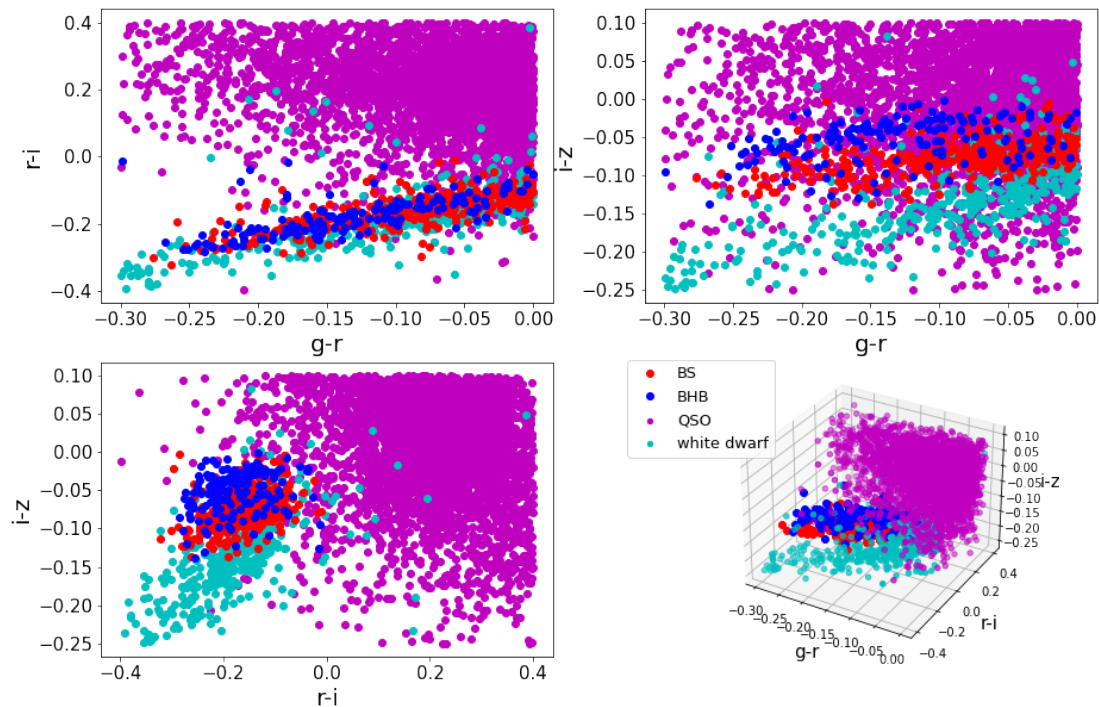


Fig. 2. The color-color diagrams for each of objects, WDs (cyan), QSOs (magenta), BSs (red) and BHBs (blue circles) in the $g-r$ vs. $r-i$ space (upper left panel), the $g-r$ vs. $i-z$ space (upper right panel) and the $r-i$ vs. $i-z$ space (lower left panel). The lower right panel shows the three dimensional diagram in the $g-r$, $r-i$ and $i-z$ colors. It follows that we can distinguish these objects in these color-color diagrams.

Figure 2 shows the locations of BHBs, BSs, WDs and QSOs in the color-color diagrams defined with g , r , i and z -band. It follows that we can separate QSOs from other objects using $r-i$ color and classify BHBs, BSs and WDs using $i-z$ color, as mentioned in the previous subsection.

Next, we use these distributions of different objects in the color-color diagrams for the application of a Bayesian method described in Fukushima et al. (2019). We construct the probability distribution function, $p(griz | \text{Comp})$, for each population ($\text{Comp} = \text{QSO, WD, BHB, BS}$ and galaxy) in terms of the mixture of several Gaussian distributions. For this purpose, we use an extreme deconvolution Gaussian mixture model (XDGM²; Bovy et al. (2011) and Holoiën et al. (2017)) with Python module.

Also to reduce contamination effect of galaxies, we use the same function and fitting parameters for the fraction of stars classified as HST/ACS among HSC-classified stars and we fit this fraction with the following function:

$$P_{\text{star}}(i) = \frac{1}{1 + \exp(ai + b)}, \quad (2)$$

where i represent i -band magnitude and (a, b) are the free parameters.

2.4 Distance estimates and spatial distributions for sample objects

In addition to the probability distribution in the color-color diagrams, we require the density distribution for each population as functions of the g -band magnitude and spatial coordinates.

For both QSOs and galaxies, we assume, for simplicity, a constant density distribution without depending on the g -band magnitude and spatial coordinates, although there may exist some large scale structures.

For WDs, we adopt a disk-like spatial distribution given by Jurić et al. (2008), as also used by Deason et al. (2014), which assumes an exponential profile and has contributions from thin and thick disk populations. Using the cylindrical coordinates (R, z) ,

² <https://github.com/tholoiën/XDGM>

$$\begin{aligned}\rho_{\text{thin}} &= \exp(R_0/L_1)\exp(-R/L_1 - |z + z_0|/H_1) \\ \rho_{\text{thick}} &= \exp(R_0/L_2)\exp(-R/L_2 - |z + z_0|/H_2) \\ \rho_{\text{disk}} &= \rho_{\text{thin}} + \rho_{\text{thick}},\end{aligned}\quad (3)$$

where $H_1 = 0.3$ kpc, $L_1 = 2.6$ kpc, $H_2 = 0.9$ kpc, $L_2 = 3.6$ kpc, $z_0 = 0.025$ kpc, $R_0 = 8.5$ kpc. An absolute magnitude for WDs is taken from the model made by Deason et al. (2014) with $\log(g_s) = 8.0(7.5)$:

$$M_g^{\text{WD}} = 12.249 + 5.101(g - r), \quad (4)$$

where the error is given as $\sigma_{M_g^{\text{WD}}} \simeq 0.5$ mag.

For the density distributions of BHBs and BSs, we assume several models and estimate the associated parameters. Considering that an axially symmetric broken power-law was the best function in Fukushima et al. (2019), the functions used for this fitting are shown below;

- Axially symmetric single power-law (ASPL)

$$\rho_{\text{halo}}(r_q) \propto r_q^{-\alpha}, \quad r_q^2 = x^2 + y^2 + z^2 q^{-2}, \quad (5)$$

where q denotes the axis ratio.

- Axially symmetric broken power-law (ABPL)

$$\rho_{\text{halo}}(r_q) \propto \begin{cases} r_q^{-\alpha_{\text{in}}} & r_q \leq r_b \\ r_q^{-\alpha_{\text{out}}} & r_q > r_b \end{cases} \quad (6)$$

In addition to these models, we also adopt a model with varying flattening, $q(r)$, which was utilized in Hernitschek et al. (2018) and Thomas et al. (2018).

- Axially symmetric single power-law with varying flattening (ASPL with $q(r)$)

$$\rho_{\text{halo}}(r_q) \propto r_q^{-\alpha}, \quad (7)$$

$$r_q^2 = x^2 + y^2 + z^2 q(r)^{-2}, \quad (8)$$

$$r^2 = x^2 + y^2 + z^2, \quad (9)$$

$$q(r) = q_\infty - (q_\infty - q_0) \exp\left(1 - \frac{\sqrt{r^2 + r_0^2}}{r_0}\right) \quad (10)$$

where q_0 is the flattening at the central region of the halo, and q_∞ is the flattening at large Galactocentric distance. r_0 is a characteristic radius marking a change between these values.

To obtain distance estimates for BHBs, we adopt the formula for their g -band absolute magnitudes, M_g^{BHB} , calibrated by Deason et al. (2011),

$$\begin{aligned}M_g^{\text{BHB}} &= 0.434 - 0.169(g_{\text{SDSS}} - r_{\text{SDSS}}) \\ &\quad + 2.319(g_{\text{SDSS}} - r_{\text{SDSS}})^2 \\ &\quad + 20.449(g_{\text{SDSS}} - r_{\text{SDSS}})^3 \\ &\quad + 94.517(g_{\text{SDSS}} - r_{\text{SDSS}})^4,\end{aligned}\quad (11)$$

where both g and r -band magnitudes are corrected for interstellar absorption. To estimate the absolute magnitude of BHBs selected from the HSC-SSP data, we use

Equations (13) - (16) below to translate HSC to SDSS filter system. We then estimate the heliocentric distances and the three dimensional positions of BHBs in rectangular coordinates, (x, y, z) , for the Milky Way space, where the Sun is assumed to be at (8.5,0,0) kpc.

The main results of our work remain unchanged by adopting the other values of of the Galactocentric distance of the Sun within the assumed observational uncertainties (7.5 kpc: e.g. Francis & Anderson (2014), 8.5 kpc: e.g. Schönrich (2012)). The vertical position of the Sun with respect to the Galactic disk is also uncertain, but it is estimated to be smaller than 50 pc and thus negligible for the purpose of this work (Karim & Mamajek 2017; Iorio et al. 2018; Hernitschek et al. 2018).

To consider the finite effect of contamination from BS stars as shown below, we adopt their g -band absolute magnitudes, M_g^{BS} , given by Deason et al. (2011),

$$M_g^{\text{BS}} = 3.108 + 5.495(g_{\text{SDSS}} - r_{\text{SDSS}}). \quad (12)$$

where the typical error is $\sigma_{M_g^{\text{BS}}} \simeq 0.5$.

To estimate their absolute magnitudes, we convert the current HSC filter system to the SDSS one by the formula given as Homma et al. (2016)

$$g_{\text{HSC}} = g_{\text{SDSS}} - a(g_{\text{SDSS}} - r_{\text{SDSS}}) - b \quad (13)$$

$$r_{\text{HSC}} = r_{\text{SDSS}} - c(r_{\text{SDSS}} - i_{\text{SDSS}}) - d \quad (14)$$

$$i_{\text{HSC}} = i_{\text{SDSS}} - e(r_{\text{SDSS}} - i_{\text{SDSS}}) + f \quad (15)$$

$$z_{\text{HSC}} = z_{\text{SDSS}} + g(i_{\text{SDSS}} - z_{\text{SDSS}}) - h, \quad (16)$$

where $(a, b, c, d, e, f, g, h) = (0.074, 0.011, 0.004, 0.001, 0.106, 0.003, 0.006, 0.006)$ and the subscript HSC and SDSS denote the HSC and SDSS system, respectively. These formula have been calibrated from both filter curves and spectral atlas of stars (Gunn & Stryker 1983).

Defining the likelihood as described in Fukushima et al. (2019), we estimate parameters for density distributions of BHBs and BSs using Goodman & Weare's Affine Invariant Markov chain Monte Carlo (MCMC) (Goodman & Weare 2010), which makes use of the Python module emcee³ (Foreman-Mackey et al. 2013) and judge these models based on bayesian information criterion (BIC). We assume that the prior distribution for model parameters is uniform over the range enough to not limit the results (see Table 2).

3 Results

In this section, we show our main results following the Bayesian method shown in Section 2 and compare with our previous work based on the different method for the

³ <https://github.com/dfm/emcee>

Table 2. Prior distribution for model parameters

Model	BHB	BS	f_{BHB}	f_{WD}	f_{QSO}
ASPL	$\alpha = 2-10, q = 0.1-4$	$\alpha = 2-10, q = 0.1-4$	0-1	0-1	0-1
ABPL	$\alpha_{\text{in}} = 2-10, \alpha_{\text{out}} = 2-10$ $r_{\text{b}}/\text{kpc} = 50-400, q = 0.1-4$	$\alpha_{\text{in}} = 2-10, \alpha_{\text{out}} = 2-10$ $r_{\text{b}}/\text{kpc} = 20-200, q = 0.1-4$	0-1	0-1	0-1
ASPL with $q(r)$	$\alpha = 2-10, r_0/\text{kpc} = 50-400$ $q_0 = 0.1-4, q_{\infty} = 0.1-4$	$\alpha = 2-10, r_0/\text{kpc} = 20-200$ $q_0 = 0.1-4, q_{\infty} = 0.1-4$	0-1	0-1	0-1

Table 3. Best fit parameters

Model	BHB	BS	f_{BHB}	f_{WD}	f_{QSO}	ΔBIC
ASPL	$\alpha = 4.11^{+0.18}_{-0.18}, q = 1.47^{+0.30}_{-0.33}$	$\alpha = 4.19^{+0.09}_{-0.08}, q = 1.36^{+0.11}_{-0.11}$	$0.192^{+0.021}_{-0.022}$	$0.879^{+0.004}_{-0.004}$	$0.279^{+0.005}_{-0.005}$	0
ABPL	$\alpha_{\text{in}} = 3.90^{+0.24}_{-0.3}, \alpha_{\text{out}} = 9.1^{+6.8}_{-3.6}$ $r_{\text{b}}/\text{kpc} = 184^{+118}_{-66}, q = 1.56^{+0.34}_{-0.23}$	$\alpha_{\text{in}} = 4.17^{+0.10}_{-0.10}, \alpha_{\text{out}} = 11.7^{+5.4}_{-4.8}$ $r_{\text{b}}/\text{kpc} = 128^{+34}_{-28}, q = 1.35^{+0.11}_{-0.10}$	$0.190^{+0.022}_{-0.022}$	$0.881^{+0.005}_{-0.005}$	$0.279^{+0.005}_{-0.004}$	26
ASPL with $q(r)$	$\alpha = 3.77^{+0.32}_{-0.40}, r_0/\text{kpc} = 189^{+128}_{-93}$ $q_0 = 1.67^{+0.48}_{-0.30}, q_{\infty} = 0.62^{+0.62}_{-0.40}$	$\alpha = 4.09^{+0.15}_{-0.15}, r_0/\text{kpc} = 130^{+45}_{-45}$ $q_0 = 1.42^{+0.14}_{-0.12}, q_{\infty} = 0.62^{+0.62}_{-0.40}$	$0.193^{+0.002}_{-0.002}$	$0.880^{+0.006}_{-0.005}$	$0.279^{+0.005}_{-0.004}$	22

selection of BHBs using the S21A data of HSC-SSP. As a result of applying the selection in Equation (1) and excluding regions that overlapped with the known structures, we finally used 42,420 stars in our analysis. As already mentioned, this sample includes BHBs, BSs, WDs, and QSOs.

3.1 Best fit models for all sample

Table 3 shows the best fit parameters for the models of ASPL and ABPL density profiles, respectively. The difference in the BIC values relative to that for the best fit case (ASPL) is also listed in the last column and it is defined ΔBIC . Figures 3 shows the MCMC results for these models. We note that as given in Equation (1), these results correspond to the sample with the magnitude range of $18.5 < g < 24.5$, suggesting BHBs at about $r = 36 \sim 575$ kpc and BSs at about $r = 16 \sim 215$ kpc. The main properties of the results are summarized as follows.

- Any power-law models reveal similar index values, i.e., BHBs are fitted to density profiles with $\alpha = 3.77^{+0.32}_{-0.40} \sim 4.11^{+0.18}_{-0.18}$, whereas BSs show somewhat steeper density profiles of $\alpha = 4.09^{+0.15}_{-0.15} \sim 4.19^{+0.09}_{-0.08}$.
- For BHBs, double power-law models (ABPL) show slightly shallower profiles at $r < r_{\text{b}}$ than the corresponding single power-law models (ASPL) expressed as $\alpha_{\text{in}} < \alpha$. For BSs, α_{in} is basically the same as α within the 1σ error.
- Both ASPL and ABPL suggest a prolate shape of $q = 1.47^{+0.30}_{-0.33}$ and $1.56^{+0.34}_{-0.23}$, respectively.
- ASPL with $q(r)$ also suggests that the MW halo has a prolate shape of $q = 1.67^{+0.48}_{-0.30}$ at its central region and an oblate shape of $q = 0.62^{+0.62}_{-0.40}$ at large r .
- ASPL provides the lower BIC than ABPL.
- The best-fit parameters for calculating the fractions of the populations, f_{BHB} , f_{WD} and f_{QSO} are basically the

same for different models. We then obtain the fraction of each population ($\tilde{f}_{\text{BHB}}, \tilde{f}_{\text{WD}}, \tilde{f}_{\text{QSO}}$), which are defined in Eqs.(18)-(20) in Fukushima et al. (2019), as $\tilde{f}_{\text{BHB}} = 0.0190 - 0.0192$, $\tilde{f}_{\text{WD}} = 0.0879 - 0.0881$ and $\tilde{f}_{\text{QSO}} = 0.279$.

3.2 Best fit models for north and south parts of the MW

We divide the data into the north and south parts of the MW and derive the optimal parameters for ASPL and ABPL models of both parts, respectively, to find any asymmetry of the density structure. For the north part, BHBs are fitted to $\alpha_{\text{in}} \simeq 4.11$, whereas BSs show a steeper density profile of $\alpha_{\text{in}} \simeq 4.47$. On the other hand, we obtain $\alpha_{\text{in}} \simeq 3.52$ for BHBs, $\alpha_{\text{in}} \simeq 3.67$ for BSs, in the south part. The MCMC results for these models are shown in Figures 4. The results given above are also tabulated in Table 4 and the main results are summarized as follows.

- The inner regions of both BHBs and BSs are steeper in the north than the south part of the MW.
- Both north and south parts show very steep profiles of α_{out} at distances exceeding $r_{\text{b}} = 100 \sim 200$ kpc.
- The south part shows $q = 1.44 \sim 2.0$, suggesting a quite prolate shape compared to the north part.
- The south part has a larger fraction of BHBs ($f_{\text{BHB}} = 0.26 \sim 0.27$) than the north part ($f_{\text{BHB}} = 0.15 \sim 0.16$), suggesting a larger number density of field halo stars in the south part.

This signature of asymmetry, especially a more prolate shape and more enhanced fraction of BHBs in the south part, may be associated with the disturbing effect of the massive Large Magellanic Cloud (e.g. Garavito-Camargo et al. 2019; Garavito-Camargo et al. 2021; Erkal et al. 2021).

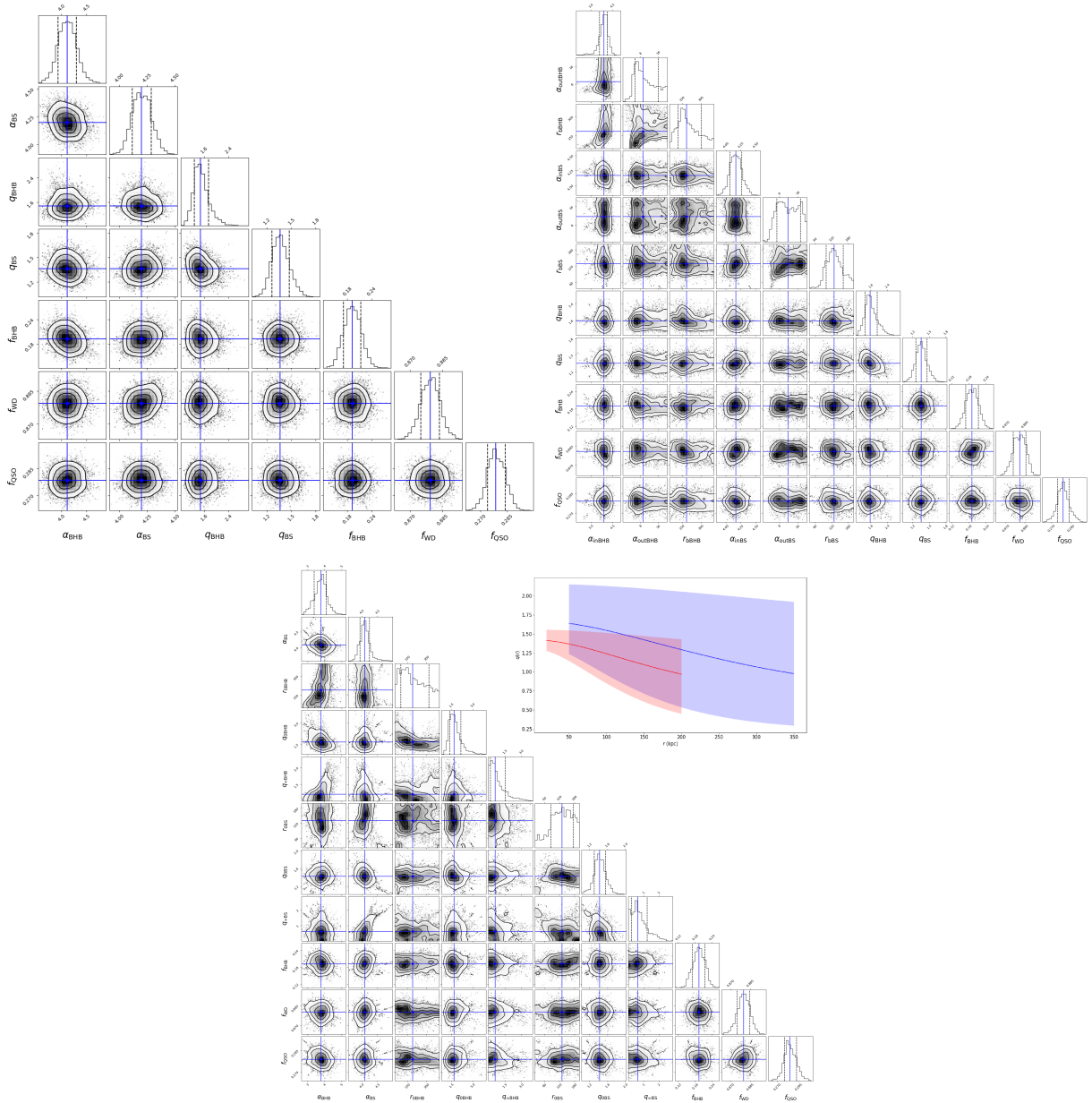


Fig. 3. MCMC results for ASPL (upper left panel), ABPL (upper right panel) and ASPL with $q(r)$ (lower panel).

3.3 Comparison with our previous work

In our previous paper (Fukushima et al. 2019), we selected candidate BHBs in the range of $18.5 < g < 23.5$ from the S18A data of HSC-SSP over $\sim 550 \text{ deg}^2$ and analyzed them using the same method as adopted in this work. The results using the S18A data (Fukushima et al. 2019) are summarised as $\alpha = 3.96^{+0.20}_{-0.16}$ and $q = 1.68^{+0.30}_{-0.33}$ for ASPL and $\alpha_{\text{in}} = 2.92^{+0.33}_{-0.33}$, $\alpha_{\text{out}} = 15.0^{+3.7}_{-4.5}$, $q = 1.72^{+0.44}_{-0.28}$ and $r_b \sim 160^{+18}_{-19}$ kpc for ABPL. It is interesting to note that (α, q) for ASPL model of the current data (S21A) are basically the same as those of the S18A data, whereas

$\alpha_{\text{in}} (= 3.88)$ for ABPL model of the current data is steeper than that of the S18A data and has instead being closer to $\alpha (= 4.02)$ for ASPL model. This suggests that the global density profile of candidate BHBs can be expressed as r^{-4} , having a boundary at $r_b \simeq 200$ kpc with a prolate shape of $q \simeq 1.5 - 1.7$. In Fukushima et al. (2019), ABPL was considered as the best model, but in the current work, ASPL is found to be the best model. We think that this is due to the difference in the magnitude range, where this work includes fainter stars ($g < 24.5$) than in the previous work ($g < 23.5$). As proof of this, when we analyze the sample

Table 4. Best fit parameters

Direction	Model	BHB	BS	f_{BHB}	f_{WD}	f_{QSO}	ΔBIC
North	ASPL	$\alpha = 4.34^{+0.36}_{-0.31}, q = 1.45^{+0.38}_{-0.27}$	$\alpha = 4.50^{+0.11}_{-0.11}, q = 1.22^{+0.09}_{-0.09}$	$0.156^{+0.026}_{-0.026}$	$0.892^{+0.006}_{-0.006}$	$0.275^{+0.005}_{-0.006}$	0
	ABPL	$\alpha_{\text{in}} = 4.11^{+0.48}_{-0.52}, \alpha_{\text{out}} = 13.6^{+9.0}_{-6.7}$ $r_{\text{b}}/\text{kpc} = 145^{+115}_{-39}, q = 1.55^{+0.51}_{-0.33}$	$\alpha_{\text{in}} = 4.47^{+0.14}_{-0.12}, \alpha_{\text{out}} = 16.3^{+9.4}_{-8.5}$ $r_{\text{b}}/\text{kpc} = 156^{+26}_{-34}, q = 1.20^{+0.09}_{-0.08}$	$0.142^{+0.025}_{-0.022}$	$0.893^{+0.005}_{-0.005}$	$0.275^{+0.006}_{-0.006}$	35
South	ASPL	$\alpha = 3.85^{+0.27}_{-0.24}, q = 2.31^{+1.00}_{-0.72}$	$\alpha = 3.79^{+0.16}_{-0.15}, q = 1.56^{+0.64}_{-0.43}$	$0.267^{+0.041}_{-0.043}$	$0.861^{+0.008}_{-0.009}$	$0.275^{+0.008}_{-0.008}$	0
	ABPL	$\alpha_{\text{in}} = 3.52^{+0.29}_{-0.31}, \alpha_{\text{out}} = 18.2^{+7.3}_{-8.2}$ $r_{\text{b}}/\text{kpc} = 196^{+46}_{-38}, q = 2.02^{+1.11}_{-0.62}$	$\alpha_{\text{in}} = 3.67^{+0.18}_{-0.16}, \alpha_{\text{out}} = 16.7^{+8.1}_{-8.6}$ $r_{\text{b}}/\text{kpc} = 118^{+38}_{-26}, q = 1.44^{+0.58}_{-0.36}$	$0.271^{+0.040}_{-0.039}$	$0.863^{+0.009}_{-0.009}$	$0.280^{+0.009}_{-0.008}$	8

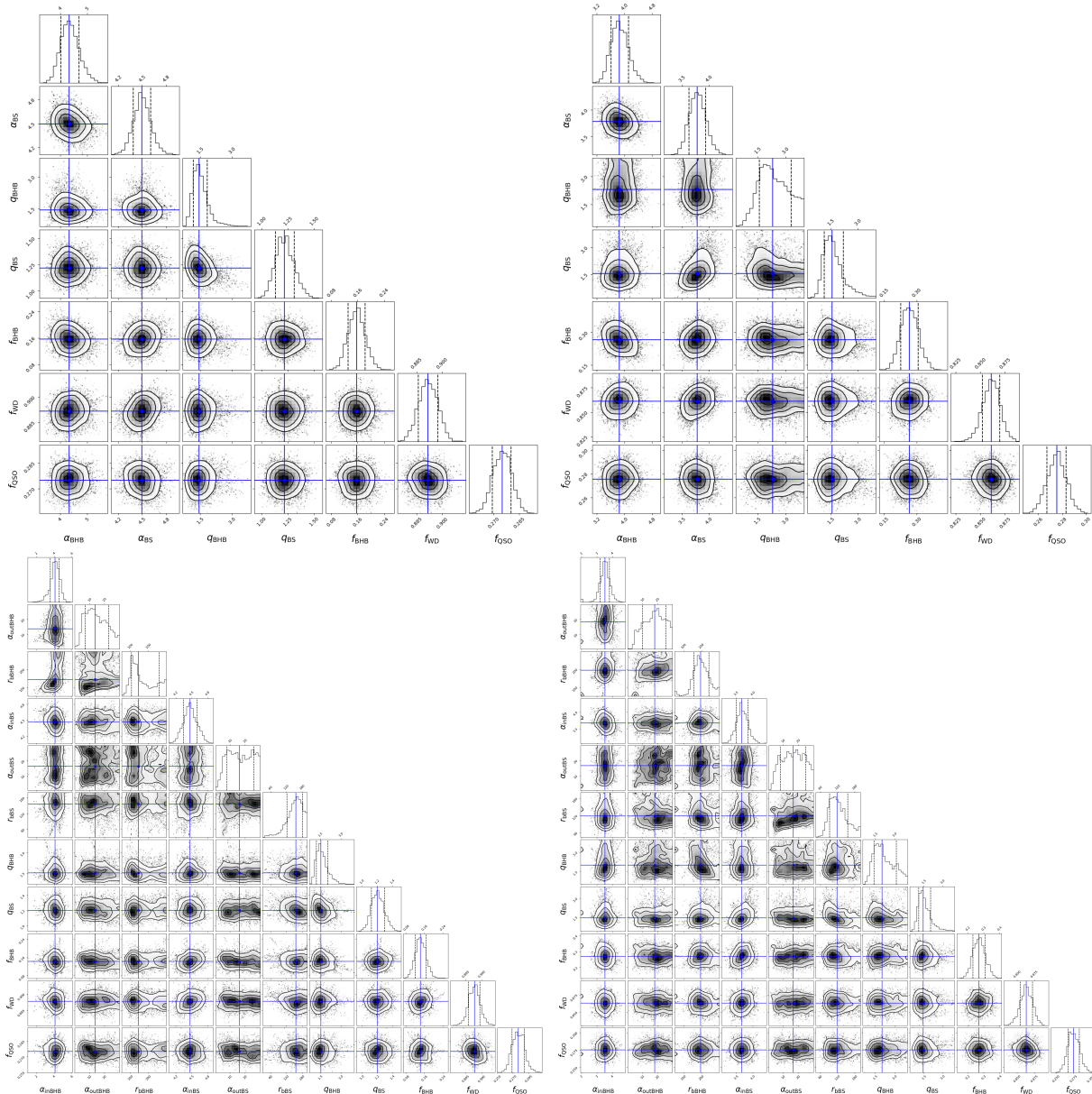


Fig. 4. MCMC results for the north (left) and south sides (right panel) of the Milky Way.

up to the same brightness as the previous work, we find that model ABPL is the best model.

3.4 Three-dimensional maps of BHBs and BSs

Given that the parameters f_{BHB} , f_{WD} and f_{QSO} basically remain the same among different density models, it is possible to derive the probability that a given target is either of a BHB, BS, WD, QSO or galaxy. For instance, the probability of a BHB is given as

$$p(\text{BHB}|x) = \frac{p(x|\text{BHB})f_{\text{BHB}}}{\sum_{i=1}^4 p(x|A_i)\tilde{f}_i + p(x|\text{galaxy})\frac{1-P_{\text{star}}}{P_{\text{star}}}}, \quad (17)$$

where x shows each sample and i denotes a component (BHB, BS, WD and QSO).

Figure 5 (with scales of $-500 \leq x, y, z \leq 500$ kpc and $-150 \leq x, y, z \leq 150$ kpc in left and right panels, respectively) show the three-dimensional maps for the sample with $p(\text{BHB}|x)$ larger than 70% (blue points) and $p(\text{BS}|x)$ larger than 70% (red points) using all the survey fields. As is clear from these figures, there are known substructures (as noted in Fukushima et al. 2019), the Sgr stream at $(x, y, z) = (-20, 10, 40)$ kpc, Sextans dSph at $(x, y, z) = (40, 60, 60)$ kpc, and the overdensity at $(x, y, z) = (0, -40, -50)$ kpc. It is also worth noting that the distribution of candidate BHBs is largely extended beyond $r \sim 150$ kpc as inferred from Figure 5.

Figure 6 shows the radial density profiles of BHBs (blue dots) and BSs (red dots) obtained in this work, where the dots (cross points) correspond to these stars having probabilities larger than 80% (70%), namely $p(\text{BHB}|x) > 0.8$ and $p(\text{BS}|x) > 0.8$ ($p(\text{BHB}|x) > 0.7$ and $p(\text{BS}|x) > 0.7$). In 80% (70%) of cases, the number of samples selected as BHB are 225 (535) and the number of samples selected as BS are 915 (1,850). Among these BHBs, the total numbers beyond 100 kpc in all observed fields and the selected fields (for deriving the global density profile) are 80 (205) and 42 (99), respectively. For comparison, the survey results of halo tracers in other works are also shown in this figure and will be discussed below.

4 Discussion

4.1 Comparison with other survey results

As mentioned in Section 1, the structure of the MW stellar halo has been studied based on the surveys of several halo tracers, as highlighted in Figure 6.

According to recent researches on the same tracer, Thomas et al. (2018) selected BHBs from their combined dataset of the deep u -band imaging from the new CFIS and the $griz$ bands from Pan-STARRS 1 covering a to-

tal of 4,000 deg² of the northern sky and revealed that a broken power-law model with an inner/outer slope of 4.24/3.21 at a break radius of 41.4 kpc is the best fitting case out to $r \sim 220$ kpc. This outer slope is somewhat shallower than the current result in the corresponding radial interval, i.e., the inner slope of $\simeq 3.90$ in our ABPL model for all samples. On the other hand, their result is similar to our case when the sample is limited to the south part of the MW, i.e., the inner slope of $\simeq 3.52$ in our ABPL model at $r < r_b \simeq 173$ kpc. Therefore, the results may slightly depend on the sampling area. In more recent research, Yu et al. (2024) revealed power law index $\alpha = 4.28$ for stellar halo within a distance range of 20 to 70 kpc using $griz$ photometry data from the Dark Energy Survey Data Release 2 (DES DR2).

The surveys using RRLs at r as large as 100 kpc tend to provide different density slopes (Watkins et al. 2009; Cohen et al. 2017; Hernitschek et al. 2018). These works show $\alpha = 4.0 \sim 4.5$ at $r > 25$ kpc, which is systematically steeper than the slopes obtained here for BHBs, but consistent with those for BSs located at similar radii to the sample of RRLs ($\alpha \simeq 4.50$ for ASPL, $\alpha_{\text{out}} \simeq 4.22$ for ABPL). Stringer et al. (2021) revealed that a broken power-law model with $\alpha_{\text{in}} \simeq 2.54$, $\alpha_{\text{out}} \simeq 5.42$, and $r_b = 32.1$ kpc is the best fitting case for RRLs from the full six-year data set of the Dark Energy Survey, which covers 5,000 deg² of the southern sky out to $r = 335$ kpc. Medina et al. (2024) reported similar results as a break in the RRLs distribution at 18.1 kpc, with an inner slope of 2.05, and a steeper outer slope of 4.47, using Dark Energy Camera data from the High cadence Transient Survey (HiTS) and the Halo Outskirts With Variable Stars (HOWVAST) survey.

According to the above studies, the density slope of RRLs is a little steeper than that of BHBs. This is comparable to the same difference between the results using BHBs and BSs, and this difference between halo tracers may be due to the process of their formation associated with merging/accretion as discussed below.

It is also worth noting that even beyond the broken radius, there exist some candidate BHBs in the outskirts, whereby producing a trough around $r \sim 200$ kpc in the density profile. While the origin of these candidate BHBs is not clear because of their small number, they might be associated with the debris of tidally disrupt dwarf galaxies or they might be just incompletely remaining contaminants such as distant faint galaxies. To settle this point, further deep surveys over much larger areas, such as the LSST survey, is needed by increasing the sample of candidate BHBs.

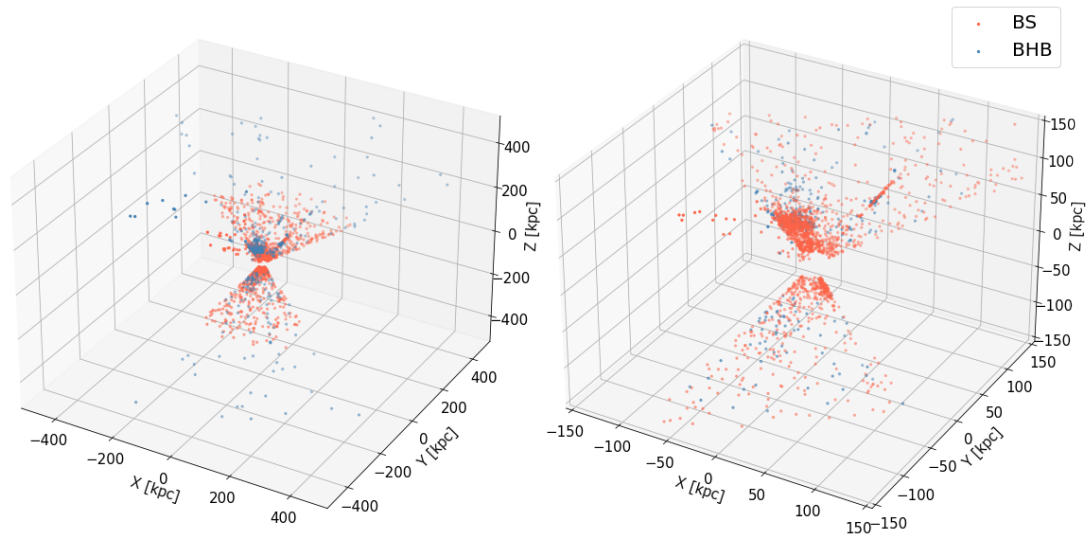


Fig. 5. Three-dimensional distributions of BHBs (blue points) and BSs (red points) selected from those having high probabilities as BHBs [$p(\text{BHB}|x) > 0.7$] and BSs [$p(\text{BS}|x) > 0.7$], respectively, as defined in Equation (17). The left panel shows the box over $-500 \leq x, y, z \leq 500$ kpc. The right panel shows the zoom-in view of the inner region over $-150 \leq x, y, z \leq 150$ kpc.

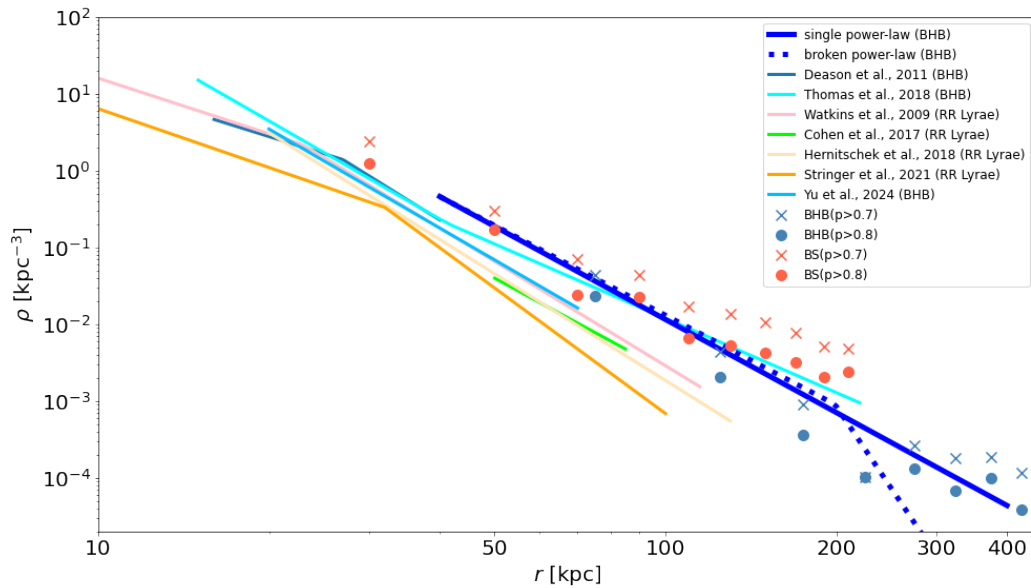


Fig. 6. Comparison of our best-fit models, the single power-law (blue solid line) and broken power-law (blue dotted line) with other works using BHBs (Deason et al. 2011; Thomas et al. 2018) and RR Lyrae (Watkins et al. 2009; Cohen et al. 2017; Hernitschek et al. 2018).

4.2 Possible constraints on the past accretion history

The current result for the spatial distribution of BHBs in the outer part of the halo, characterized by a shallower den-

sity profile than the inner part of the halo (25 – 50 kpc), provides an important constraint on the formation his-

tory of the MW. Indeed, numerical simulations for galaxy formation suggest similar halo structures, which is comprised of *in situ* and *ex situ* halo components (Zolotov et al. 2009; Zolotov et al. 2010; Oser et al. 2010; Font et al. 2011; McCarthy et al. 2012; Tissera et al. 2012; Tissera et al. 2013; Rodriguez-Gomez et al. 2016). For instance, Font et al. (2011) and McCarthy et al. (2012) found from their simulated galaxies that the inner halo formed from the *in situ* star formation mode shows a relatively steeper density profile than the outer part of the halo (*ex situ* halo), which are formed from accreted satellites. Similarly, using the Illustris Project (Genel et al. 2014; Vogelsberger et al. 2014a; Vogelsberger et al. 2014b) for the suite of hydrodynamical simulations for galaxy formation over a wide range of stellar masses, $M_* = 10^9 - 10^{12} M_\odot$, Rodriguez-Gomez et al. (2016) found that these two halo components are spatially separated, where the *in situ* (*ex situ*) halo dominates the inner (outer) part of the halo.

Indeed, as shown in Figure 10 of Rodriguez-Gomez et al. (2016) for the total stellar mass of $M_* = 10^{11} M_\odot$, i.e., like the MW-like stellar mass, the *in situ* halo component is characterized by a relatively shallow density profile over the very inner region of the halo at $r \lesssim r_{\text{half},*}$ (where $r_{\text{half},*}$ is a stellar half-mass radius) and a steep density slope over $r_{\text{half},*} \lesssim r \lesssim 4r_{\text{half},*}$, whereas the *ex situ* component at $r \gtrsim 4r_{\text{half},*}$ shows a relatively shallow density slope. This radius ($\sim 4r_{\text{half},*}$ for $M_* = 10^{11} M_\odot$) is the transition radius, where the two halo components locally become equally abundant, and this is smaller for more massive galaxies (Rodriguez-Gomez et al. 2016). It is worth noting that this behavior of the theoretically predicted halo is generally in agreement with the observed density profile of the halo probed with RRLs, BSs, and BHBs: as presented in Deason et al. (2014) (see their Figure 7), the observed halo with BHBs and BSs selected from the Sloan Digital Sky Survey (SDSS) sample shows a shallow profile at $r \lesssim 25$ kpc ($\alpha \sim 2.5$) and a steep profile over $25 \lesssim r \lesssim 100$ kpc ($\alpha = 4 \sim 6$). Deeper surveys of these halo tracers like the current work using Subaru suggest a shallow profile beyond $r \sim 100$ kpc ($\alpha \sim 4$), which is possibly the *ex situ* component originated from accretion of small stellar systems.

4.3 The color gradient of BHBs

To infer the information on the spatial distribution of ages and metallicities for BHBs (BSs), we calculate the average values and standard errors of $g-r$ colors for bins separated by 50 kpc (25 kpc). In Figure 7, we show the mean color ($g-r$) as a function of r_q for BHBs and BSs selected by $p(\text{BHB}|x) > 0.7$ and $p(\text{BS}|x) > 0.7$, respectively ($q = 1.5$ for

BHB, $q = 1.36$ for BS). We see that rapidly turning blue around 180 kpc in the color of BHBs. We adopt a t-test to check whether there is a significant difference between the overall average of the color and the average in the range of $r = 150 \sim 200$ kpc, and find that the p-value is ~ 0.018 , indicating it is statistically significant.

In previous studies, the color distribution of BHBs further inside the MW have been analyzed. For example, Preston et al. (1991) showed a color gradient out to ~ 12 kpc. Furthermore, similar results are obtained ~ 40 kpc in Santucci et al. (2015) using BHB stars selected from the SDSS sample. They detected that the mean de-reddened $g-r$ color increases outward in the Galaxy. In these studies, the trends in color gradients did not differ between samples of different metallicity, suggesting that the origin of color gradients may reflect age gradients. These may reflect that more massive systems, which would have grown over a longer timescale, are less affected by tidal forces and can fall deeper into the potential. A similar relationship between age and distance is also shown in Das et al. (2016) using BHBs from the Sloan Extension for Galactic Understanding and Exploration-II (SEGUE-II) survey. More recent studies have shown similar color and age gradients in Whitten et al. (2019) using the SDSS, Pan-STARRS1 and the cross-matched GALEX GUVCat with Pan-STARRS DR1. When compared, the color near the farthest 30 kpc is 0.14 to 0.15, which is close to the value of 0.16 of the innermost sample in our result.

4.4 On the edge of the MW's stellar halo

In the cosmological N -body simulations of Λ CDM models for structure formation in the Universe, a sharp decrease in the slope of the radial density profile is seen at the edge of the virialized dark halo, which usually appears at $r \sim 1.4r_{200}$ in a dark halo and is called a "splashback radius" (Diemer & Kravtsov 2014; More et al. 2015; Deason et al. 2020). In particular, Diemer & Kravtsov (2014) and More et al. (2015) revealed, using cosmological N -body simulations, that the splashback radius falls in the range of $(0.8-1.0) r_{200}$ for rapidly accreting halos and is $\sim 1.5r_{200}$ for slowly accreting halos. For Milky Way-mass galaxies, a sharp decrease in the density slope of the stellar halo, which called a "caustic radius", also appears in $(0.3 - 0.8) r_{200}$, which is associated with the second caustic radius of a dark halo as stated in Deason et al. (2020).

Therefore, to get insights into these characteristic radii from the current data, we attempt to fit the radial distribution of our BHB sample to the mixture of the Einasto profile (Einasto 1965) for the inner part of the halo and the power-law profile for its outermost part as defined in

Diemer & Kravtsov (2014):

$$\rho(r_q) = f_{\text{trans}}\rho_{\text{einasto}} + \rho_{\text{outer}} \quad (18)$$

$$\rho_{\text{einasto}} = \rho_0 \exp\left(-\frac{2}{n}\left[\left(\frac{r_q}{r_s}\right)^n - 1\right]\right) \quad (19)$$

$$f_{\text{trans}} = \left[1 + \left(\frac{r_q}{r_t}\right)^\beta\right]^{-\gamma/\beta} \quad (20)$$

$$\rho_{\text{outer}} = \rho_m \left[b_e \left(\frac{r_q}{5r_{200}}\right)^{-S_e} + 1\right] \quad (21)$$

$$r_q^2 = x^2 + y^2 + z^2 q^{-2}. \quad (22)$$

where the Einasto profile, ρ_{einasto} , is characterized by three parameters (n, r_s, ρ_0), and the transition term, f_{trans} , provides the steepening of the profile at around a truncation radius, r_t , where β and γ give the steepness of the profile at $r \sim r_{200}$. The outermost profile, ρ_{outer} , is given by a power-law with an index S_e plus the mean density of the universe, ρ_m .

The best-fit values for the parameters in this function form are summarized in Table 5 and the best-fit density profiles for BHBs and BSs are shown in Figure 8. For BHBs, a rapid increase in the slope between $r = 400$ kpc and 500 kpc is likely to be observed, but no clear results for a splashback/caustic radius are obtained from the current sample. On the other hand, a sharp increase in the slope is observed between $r = 200$ kpc and 300 kpc for BSs. This result is roughly consistent with the finding that the edge of the Milky Way is located at $r = 292$ kpc obtained from the motion of dwarf galaxies in Deason et al. (2020). However, as is clear from Figure 8, the current result suffers from a rather large error, so the derivation of a splashback/caustic radius is yet inconclusive in our work.

4.5 The effects of the photometric errors on the results

First, to investigate how the photometric errors affect the color distribution shown in Figure 2, we compare the $g - r$ vs. $i - z$ distribution between the sample by excluding the data with errors larger than 0.05 mag and that without this restriction in the analysis, as presented in Figure 9. It is clear that the color distribution of BHBs and BS remains the same even considering the photometric errors.

Next, we perform an additional analysis using only the samples with magnitudes of $g < 23$ (i.e., within $r = 300$ kpc) with the photometric errors smaller than 0.05 mag. The photometric errors for each band are shown in Figure 10. As presented in Table 6, we have obtained the similar results to those for the samples without this restriction shown in Section 3.1, thereby suggesting that the impact of the photometric errors on the results is limited. It is worth noting that a discontinuous change of α at a break radius r_b is more pronounced for the samples with low

photometric errors than the samples without this restriction, although the obtained r_b is different. The BIC value for ABPL is the largest, indicating that this is the optimal model. This result is understood from the fact that excluding the data with large photometric errors leads to the lack of the sample stars beyond $r = 300$ kpc, that mitigates the effect of the tendency for α to become smaller again at $r > 300$ kpc. As mentioned above, the samples at such radii contain large photometric errors, suggesting that it is necessary to compare these results with those available from future deeper surveys, as discussed in Section 4.4.

5 Conclusions

We have selected and analyzed candidate BHBs from the HSC-SSP Wide layer data obtained until 2021 January (S21A), which covers $\sim 1,100$ deg² area, based on an extensive Bayesian method to minimize the effects of non-BHB contamination as much as possible. In this selection method, the z -band brightness of a selected stellar target is useful as a probe of a surface gravity of a BHB star against other A-type stars.

Applying our selection method to the sample with $18.5 < g < 24.5$, which, for candidate BHBs, corresponds to the Galactocentric radii at $r = 36 \sim 575$ kpc, we have obtained the density slopes of BHBs for a single power-law model as $\alpha = 4.11^{+0.18}_{-0.18}$ and for a broken power-law model as $\alpha_{\text{in}} = 3.90^{+0.24}_{-0.30}$ and $\alpha_{\text{out}} = 9.1^{+6.8}_{-3.6}$ divided at a radius of $r_b = 184^{+118}_{-66}$ kpc. The difference in statistical significance between these power-law models appears small. For these models allowing a non-spherical halo shape, an axial ratio of $q = 1.56^{+0.34}_{-0.23}$ or $q = 1.35^{+0.11}_{-0.19}$ corresponding to a prolate shape is most likely. It is also suggested from the spatial distribution of the currently selected BHBs that the MW stellar halo may have a trough at around $r \sim 200$ kpc, although this needs to be assessed using the further survey data.

The density slope obtained in this work is basically in agreement with that from the CFIS survey for BHBs (Thomas et al. 2018). However, it is systematically shallower than the slope derived from RRLs at r below ~ 100 kpc (Cohen et al. 2017; Hernitschek et al. 2018). This may be simply due to the different radial range of each sample, $r < 100$ kpc for RRLs and $50 < r < 360$ kpc for BHBs, or RRLs may have an intrinsically more centrally concentrated distribution than BHBs. However, distant data contains at least some errors, and in order to understand the global structure of the MW's stellar halo, a further analysis using wider and deeper data is necessary such as with the LSST survey at the Vera Rubin Observatory and the ongoing Ultraviolet Near-Infrared Northern Sky

Table 5. Best fit parameters for Einasto model

BHB	BS	f_{BHB}	f_{WD}	f_{QSO}
$\log(\rho_0/\rho_m) = 9.7^{+1.2}_{-1.0}$, $\log(n) = -0.92^{+0.19}_{-0.25}$, $\log(r_s) = -0.13^{+0.65}_{-0.58}$, $\log(b_e) = 9.9^{+0.9}_{-1.3}$, $S_e = 9.1^{+1.1}_{-1.0}$, $\log(r_t) = 2.3^{+0.5}_{-0.4}$, $\log(\beta) = 0.14^{+0.79}_{-0.51}$, $\log(\gamma) = 0.35^{+0.53}_{-0.68}$, $\log(q) = 0.12^{+0.13}_{-0.12}$	$\log(\rho_0/\rho_m) = 11.5^{+1.1}_{-1.2}$, $\log(n) = -0.81^{+0.16}_{-0.13}$, $\log(r_s) = -0.35^{+0.60}_{-0.55}$, $\log(b_e) = 10.0^{+1.1}_{-1.0}$, $S_e = 10.2^{+0.8}_{-0.7}$, $\log(r_t) = 2.3^{+0.5}_{-0.5}$, $\log(\beta) = -0.17^{+0.81}_{-0.53}$, $\log(\gamma) = 0.22^{+0.47}_{-0.64}$, $\log(q) = 0.14^{+0.05}_{-0.06}$	$-0.210^{+0.032}_{-0.052}$	$0.882^{+0.008}_{-0.007}$	$0.279^{+0.007}_{-0.007}$

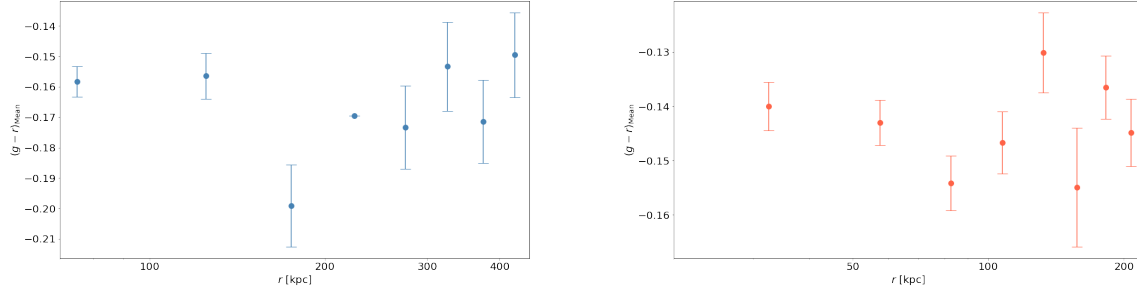


Fig. 7. The left (right) panel show the color ($g-r$) gradient of BHBs (BSs) selected by $p(\text{BHB}|x) > 0.7$ ($p(\text{BS}|x) > 0.7$). The average value of ($g-r$) for bins separated by 50 kpc (25 kpc) is plotted as the points and the bars indicate standard errors (calculated by σ/\sqrt{n} when σ is standard deviation and n is sample size). We see that rapidly turning blue around 180 kpc in the color gradient of BHBs.

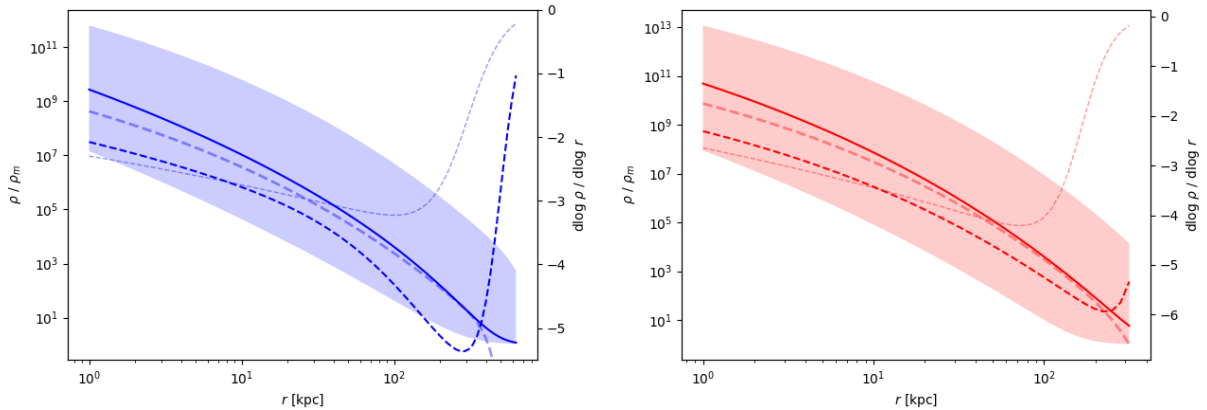


Fig. 8. The left (right) panel show the best fit results for BHBs (BSs). The blue (red) solid line is the density distribution, and the light blue (light red) shadow shows the error range. The blue (red) dashed blue line indicates the slope of the density distribution. The thick light blue (light red) dashed line shows the slope at the upper limit of the error, and the thin light blue (light red) dashed line shows the slope at the lower limit of the error.

Survey (UNIONS) that covers the footprint of the Euclid Survey (Euclid Collaboration 2022)². Also, to interpret such observational results in the form of the past merging history, more extensive numerical simulations for the formation of stellar halos will be important, where not only

accretion/merging of satellites from outside but also the *in situ* formation of halo stars are properly taken into account.

Acknowledgments

This work is supported in part by JSPS Grant-in-Aid for Scientific Research (B) (No. 25287062) and MEXT Grant-in-Aid for Scientific Research (No. 18H05437, 21H05448, and 24K00669 for MC, No. JP20H01895, JP21K13909, and

² UNIONS combines multi-band photometric images from different telescopes: u - and r -band images from CFHT called CFIS, i - and z -band from Pan-STARRS, z - and g -band from Subaru HSC called WISHES and WHIGS, respectively (WISHES: Wide Imaging with Subaru HSC of the Euclid Sky, WHIGS: Waterloo Hawai'i IFA Survey).

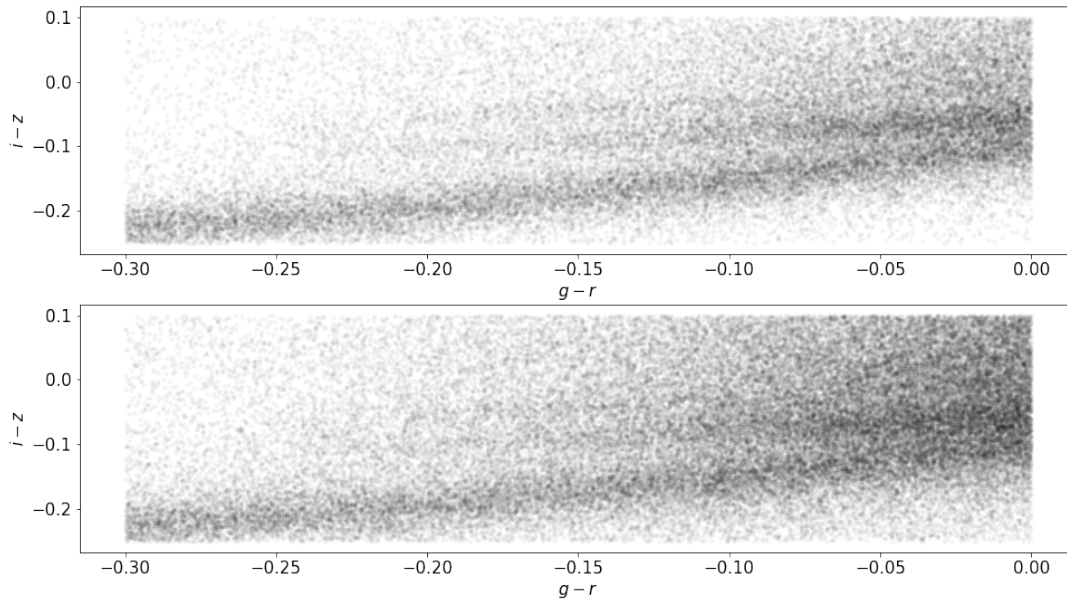


Fig. 9. The $g-r$ vs. $i-z$ diagram for S21A data by excluding the stars with g -band photometric errors exceeding 0.05 mag (upper panel) and for all the stars (lower panel).

Table 6. Best fit parameters for sample g under 23 mag

Model	BHB	BS	f_{BHB}	f_{WD}	f_{QSO}	ΔBIC
ASPL	$\alpha = 4.51^{+0.26}_{-0.25}$, $q = 1.51^{+0.04}_{-0.03}$	$\alpha = 4.63^{+0.10}_{-0.11}$, $q = 1.40^{+0.02}_{-0.02}$	$0.20^{+0.02}_{-0.02}$	$0.86^{+0.01}_{-0.01}$	$0.29^{+0.01}_{-0.01}$	76
ABPL	$\alpha_{\text{in}} = 4.12^{+0.38}_{-0.37}$, $\alpha_{\text{out}} = 16.12^{+2.64}_{-4.75}$ $r_{\text{b}}/\text{kpc} = 118^{+32}_{-18}$, $q = 1.75^{+0.50}_{-0.32}$	$\alpha_{\text{in}} = 4.35^{+0.13}_{-0.13}$, $\alpha_{\text{out}} = 16.11^{+2.51}_{-3.19}$ $r_{\text{b}}/\text{kpc} = 55^{+5}_{-4}$, $q = 1.29^{+0.11}_{-0.09}$	$0.19^{+0.02}_{-0.02}$	$0.86^{+0.01}_{-0.01}$	$0.29^{+0.01}_{-0.01}$	0
ASPL with $q(r)$	$\alpha = 4.24^{+0.40}_{-0.28}$, $r_0/\text{kpc} = 177^{+52}_{-62}$ $q_0 = 1.94^{+0.42}_{-0.38}$, $q_{\infty} = 0.52^{+0.62}_{-0.36}$	$\alpha = 4.28^{+0.32}_{-0.24}$, $r_0/\text{kpc} = 67^{+34}_{-20}$ $q_0 = 1.58^{+0.30}_{-0.21}$, $q_{\infty} = 0.50^{+0.94}_{-0.37}$	$0.20^{+0.03}_{-0.02}$	$0.86^{+0.01}_{-0.01}$	$0.29^{+0.01}_{-0.01}$	65

JP23H04009 for KH). TM is supported by a Gliese Fellowship at the Zentrum für Astronomie, University of Heidelberg, Germany.

The Hyper Suprime-Cam (HSC) collaboration includes the astronomical communities of Japan and Taiwan, and Princeton University. The HSC instrumentation and software were developed by the National Astronomical Observatory of Japan (NAOJ), the Kavli Institute for the Physics and Mathematics of the Universe (Kavli IPMU), the University of Tokyo, the High Energy Accelerator Research Organization (KEK), the Academia Sinica Institute for Astronomy and Astrophysics in Taiwan (ASIAA), and Princeton University. Funding was contributed by the FIRST program from Japanese Cabinet Office, the Ministry of Education, Culture, Sports, Science and Technology (MEXT), the Japan Society for the Promotion of Science (JSPS), Japan Science and Technology Agency (JST), the Toray Science Foundation, NAOJ, Kavli IPMU, KEK, ASIAA, and Princeton University. This paper makes use of software developed for the Large Synoptic Survey Telescope. We thank the LSST Project for making their code freely available. The Pan-STARRS1 (PS1) Surveys have been made pos-

sible through contributions of the Institute for Astronomy, the University of Hawaii, the Pan-STARRS Project Office, the Max-Planck Society and its participating institutes, the Max Planck Institute for Astronomy and the Max Planck Institute for Extraterrestrial Physics, The Johns Hopkins University, Durham University, the University of Edinburgh, Queen's University Belfast, the Harvard-Smithsonian Center for Astrophysics, the Las Cumbres Observatory Global Telescope Network Incorporated, the National Central University of Taiwan, the Space Telescope Science Institute, the National Aeronautics and Space Administration under Grant No. NNX08AR22G issued through the Planetary Science Division of the NASA Science Mission Directorate, the National Science Foundation under Grant No. AST-1238877, the University of Maryland, and Eotvos Lorand University (ELTE).

References

Abazajian, K., Adelman-McCarthy, J. K., Agüeros, M. A., et al. 2004, *AJ*, 128, 502

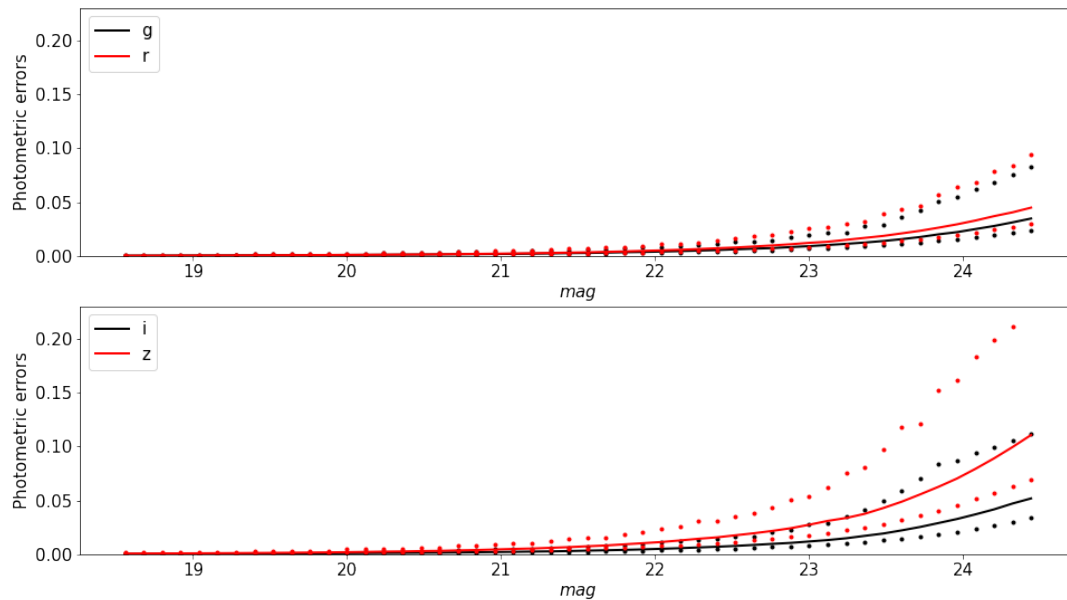


Fig. 10.

Photometric errors in the current data. The black and red lines in the upper panel are for the g-band and r-band, respectively, and the black and red lines in the lower panel are for the i-band and z-band, respectively. The dotted lines correspond to the 5% and 95% percentile data for each band and the median is shown as a solid line.

- Adhikari S., Dalal N., Chamberlan R.T., 2014, *J. Cosmology Astropart. Phys.*, 2014, 019
- Aihara, H., Arimoto, N., Bickerton, S., et al. 2018a, *PASJ*, 70, S4
- Aihara, H., Armstrong, R., Bickerton, S., et al. 2018b, *PASJ*, 70, S8
- Amarante, J. A. S., Kuposov, S. E., Laporte, C. F. P. 2024, preprint, arXiv:2404.09825
- Axelrod, T., Kantor, J., Lupton, R. H., & Pierfederici, F. 2010, in *Proc. SPIE*, Vol. 7740, *Software and Cyberinfrastructure for Astronomy*, 774015
- Bekki, K., & Chiba, M. 2001, *ApJ*, 558, 666
- Belokurov, V., Zucker, D. B., Evans, N. W., et al. 2006, *ApJL*, 647, L11
- Belokurov, V., Kuposov, S. E., Evans, N. W., et al. 2014, *MNRAS*, 437, 116
- Belokurov V., Erkal D., Evans N. W., et al. 2018, *MNRAS*, 478, 611
- Bland-Hawthorn, J., & Freeman, K., 2014, *The Origin of the Galaxy and Local Group*, Saas-Fee Advanced Course, Vol. 37 (Springer)
- Bosch, J., Armstrong, R., Bickerton, S., et al. 2018, *PASJ*, 70, S5
- Bovy J., Hogg D. W., Roweis S. T., 2011, *Annals of Applied Statistics*, 5, 1657
- Bullock, J. S. & Johnston, K. V. 2005, *ApJ*, 635, 931
- Chen, B., Stoughton, C., Smith, J. A., et al. 2001, *ApJ*, 553, 184
- Cohen, J. G., Sesar, B., Banholzer, S., the PTF Collaboration, 2015, *IAU General Assembly*, 22, 2255152
- Cohen, J. G., Sesar, B., Banholzer, S. et al. 2017, *ApJ*, 849, 150
- Cooper, A. P. et al., 2010, *MNRAS*, 406, 744
- Das, P., Williams, A., & Binney, J. 2016, *MNRAS*, 463, 3169. doi:10.1093/mnras/stw2167
- Das, P., Hawkins, K., Jofré, P. 2020, *MNRAS*, 493, 5195
- Deason, A. J., Belokurov, V., & Evans, N. W. 2011, *MNRAS*, 416, 2903
- Deason, A. J., Belokurov, V., Kuposov S. E., Rockosi C. M. 2014, *ApJ*, 787, 30
- Deason, A. J., Belokurov, V., Kuposov S. E. 2018a, *ApJ*, 852, 118
- Deason, A. J., Belokurov, V., Kuposov S. E., & Lancaster, L. 2018b, *ApJL*, 862, L1
- Deason, A. J., Fattahi, A., Frenk, C. S., et al. 2020, *MNRAS*, 496, 3929
- Diemer B., Kravtsov A. V., 2014, *ApJ*, 789, 1
- Einasto, J. 1965, *Trudy Inst. Astroz. Alma-Ata*, 5, 87
- Erkal, D., et al. 2021, *MNRAS*, 506, 267
- Euclid Collaboration, Scaramella, R., Amiaux, J., et al. 2022, *A&A*, 662, A112
- Feltzing, S., & Chiba, M. 2013, *New Astronomy Reviews*, 57, 80
- Feng, Y., Guhathakurta, G., Peng, E. W., et al. 2024, submitted to *ApJ*, arXiv:2402.05418, doi:10.48550/arXiv.2402.05418

- Font, A. S., McCarthy, I. G., Crain, R. A., et al. 2011, *MNRAS*, 416, 2802
- Foreman-Mackey D., Hogg D. W., Lang D., Goodman J., 2013, *PASP*, 125, 306
- Fukushima, T., Chiba, M., Okamoto, S., et al. 2018, *PASJ*, 70, 69
- Fukushima, T., Chiba, M., Tanaka, M., et al. 2019, *PASJ*, 71, 72
- Furusawa, H., et al. 2018, *PASJ*, 70, S3
- Francis, C. & Anderson, E. 2014, *MNRAS*, 441, 1105. doi:10.1093/mnras/stu631
- Garavito-Camargo, N., et al. 2019, *ApJ*, 884, 51
- Garavito-Camargo, N., et al. 2021, *ApJ*, 919, 109
- Genel, S., et al. 2014, *MNRAS*, 445, 175
- Goodman J., Weare J., 2010, *Comm. App. Math. Comp. Sci.*, 5, 65
- Grand, R. J. J., et al. 2017, *MNRAS*, 467, 179
- Gunn, J. E., & Stryker, L. L., 1983, *ApJS*, 52, 121
- Harris, W. E. 1996, *AJ*, 112, 1487
- Helmi, A. & White, S. D. M., 1999, *MNRAS*, 307, 495
- Helmi, A. 2008, *A&ARV*, 15, 145
- Helmi A., Babusiaux C., Koppelman H. H., et al. 2018, *Nature*, 563, 85
- Helmi, A. 2020, *A&ARV*, 58, 205
- Hernitschek, N., Cohe, J. G., Rix, H.-W., et al., 2018, *ApJ*, 859, 31
- Holoien T. W.-S., Marshall P. J., Wechsler R. H., 2017, *AJ*, 153, 249
- Homma, D., Chiba, M., Okamoto, S., et al. 2016, *ApJ*, 832, 21
- Horta, D., Schiavon, R. P., Mackereth, J. T., et al. 2021, *MNRAS*, 500, 1385
- Horta, D., Schiavon, R. P., Mackereth, J. T., et al. 2023, *MNRAS*, 520, 5671
- Ibata, R. A., Gilmore, G., Irwin, M. J. 1995, *MNRAS*, 277, 781
- Iorio, G., Belokurov, V., Erkal, D., et al. 2018, *MNRAS*, 474, 2142. doi:10.1093/mnras/stx2819
- Ivezić, Z., Axelrod, T., Brandt, W. N., et al. 2008, *AJ*, 176, 1
- Ivezić, Ž., Kahn, S. M., Tyson, J. A., et al. 2019, *ApJ*, 873, 111. doi:10.3847/1538-4357/ab042c
- Ivezić, Z., Beers, T. C., & Jurić, M. 2012, *ARAA*, 50, 251
- Jurić, M., Ivezić, Z., Brooks, A., et al. 2008, *ApJ*, 673, 864
- Jurić, M., Kantor, J., Lim, K.-T., et al. 2017, *ASPC*, 512, 279
- Karim, T. & Mamajek, E. E. 2017, *MNRAS*, 465, 472. doi:10.1093/mnras/stw2772
- Kawanomoto, S. et al. 2018, *PASJ*, 70, 66
- Keller, S. C., Murphy, S., Prior, S., Da Costa, G., & Schmidt, B. 2008, *ApJ*, 678, 851
- Kepler, S. O., Pelisoli, I., Koester, D., et al. 2015, *MNRAS*, 446, 4078
- Kepler, S. O., Pelisoli, I., Koester, D., et al. 2016, *MNRAS*, 455, 3413
- Kleinman, S. J., Kepler, S. O., Koester, D., et al. 2013, *ApJS*, 204, 5
- Komiyama, Y., et al. 2018, *PASJ*, 70, S2
- Lee, Y. S., Beers, T. C., Sivarani, T., et al. 2008, *AJ*, 136, 2022.
- Lenz, D. D., Newberg, J., Rosner, R., et al. 1998, *ApJS*, 119, 121
- Magnier, E. A., Schlafly, E., Finkbeiner, D., et al. 2013, *ApJS*, 205, 20
- Malhan, K., Yuan, Z., Ibata, R. A., et al. 2021, *ApJ*, 920, 51
- Matsuno, T., Dodd, E., Koppelman, H. H., et al. 2022, *ã*, 665, 46
- McCarthy, I. G., Font, A. S., Crain, R. A., et al. 2012, *MNRAS*, 420, 2245
- McConnachie, A. W. 2012, *AJ*, 144, 4
- Medina, G. E., Muñoz, R. R., Carlin, J. L., et al. 2024, submitted to *MNRAS*, arXiv:2402.14055. doi:10.48550/arXiv.2402.14055
- Miyazaki, S., Komiyama, Y., Kawanomoto, S. et al. 2018, *PASJ*, 70, S1
- Monachesi, A. et al. 2018, *MNRAS*, 485, 2589
- More S., Diemer B., Kravtsov A. V., 2015, *ApJ*, 810, 36
- Newberg, H. J., & Yanny, B. 2005, *JPhCS*, 47, 195
- Oser, L., Ostriker, J. P., Naab, T., et al. 2010, *ApJ*, 725, 2312
- Pâris I. et al. 2018, *A&A*, 613, A51
- Pillepich, A., Vogelsberger, M., Deason, A., et al. 2014, *MNRAS*, 244, 237
- Preston, G. W., Shectman, S. A., & Beers, T. C. 1991, *ApJ*, 375, 121. doi:10.1086/170175
- Rey, M. P., & Starkenburg, T. K. 2022, *MNRAS*, 510, 4208
- Rodriguez-Gomez, V., Pillepich, A., Sales, L. V. et al. 2016, *MNRAS*, 458, 2371
- Santucci, R. M., Beers, T. C., Placco, V. M., et al. 2015, *ApJL*, 813, L16. doi:10.1088/2041-8205/813/1/L16
- Schlafly, E. F., & Finkbeiner, D. P. 2011, *ApJ*, 737, 103
- Schlafly, E. F., Finkbeiner, D. P., Jurić, M., et al. 2012, *ApJ*, 756, 158
- Schönrich, R. 2012, *MNRAS*, 427, 274. doi:10.1111/j.1365-2966.2012.21631.x
- Sesar, B., Jurić, M., & Ivezić, Z. 2011, *ApJ*, 731, 4
- Sirko, E., Goodman, J., Knapp, G. R., et al. 2004, *AJ*, 127, 899
- Slater, C. T., Nidever, D. L., Munn, J. A., Bell, E. F., & Majewski, S. R. 2016, *ApJ*, 832, 206
- Sluis, A. P. N., & Arnold, R. A. 1998, *MNRAS*, 297, 732
- Stringer K. M., et al., 2021, *ApJ*, 911, 109
- Suzuki, Y., Chiba, M., Komiyama, Y., et al. 2024, *PASJ*, 76, 205
- Tissera, P. B., White, S. D. M., Scannapieco, C., 2012, *MNRAS*, 420, 255
- Tissera, P. B., Scannapieco, C., Beers, T.C., Carollo, D., 2013, *MNRAS*, 432, 3391
- Thomas, G. A., McConnachie, A. W., Ibata, R. A., et al. 2018, *MNRAS*, 481, 5223
- Tonry, J. L., Stubbs, C. W., Lykke, K. R., et al. 2012, *ApJ*, 750, 99
- Vickers, J. J., Grebel, E. K., & Huxor, A. P. 2012, *AJ*, 143, 86
- Vivas, A. K., Zinn, R., Farmer, J., et al. 2016, *ApJ*, 831, 165
- Vogelsberger, M. et al. 2014a, *Nature*, 509, 177
- Vogelsberger, M. et al. 2014b, *MNRAS*, 444, 1518
- Watkins, L. L. et al. 2009, *MNRAS*, 398, 1757
- White, S. D. M., & Rees, M. J. 1978, *MNRAS*, 183, 341
- Whitten, D. D., Beers, T. C., Placco, V. M., et al. 2019, *ApJ*, 884, 67. doi:10.3847/1538-4357/ab4269
- Xu, Y., Liu, C., Xue, X.-X., et al. 2018, *MNRAS*, 473, 1244

- Xue, X.-X., Rix, H.-W., Yanny, B., et al. 2011, *ApJ*, 738, 79
- Yanny, B., Newberg, H. J., Kent, S., et al. 2000, *ApJ*, 540, 825
- Yu, F., Li, T. S., Speagle, J. S., et al. 2024, preprint,
arXiv:2402.00104. doi:10.48550/arXiv.2402.00104
- Zolotov, A., Willman, B., Brooks, A. M., et al. 2009, *ApJ*, 702,
1058
- Zolotov, A., Willman, B., Brooks, A. M., et al. 2010, *ApJ*, 721,
738